energies

MDPI

Article

Analysis of Sliding-Mode Controlled Impedance Matching Circuits for Inductive Harvesting Devices

Juan A. Garriga-Castillo [1], Hugo Valderrama-Blavi [2,*], José A. Barrado-Rodrigo [2] and Àngel Cid-Pastor [2]

1 Department of Informatics and Industrial Engineering, Universitat de Lleida, c/Jaume II, 69.25001 Lleida, Spain; garriga@diei.udl.es

2 Laboratory GAEI, ETSE-Universitat Rovira i Virgili, Av. Països Catalans 26, 43007 Tarragona, Spain; joseantonio.barrado@urv.cat (J.A.B.-R.); angel.cid@urv.cat (À.C.-P.)

* Correspondence: hugo.valderrama@urv.cat; Tel.: +34-977-558-523

Received: 3 September 2019; Accepted: 6 October 2019; Published: 12 October 2019

Abstract: A sea-wave energy harvesting, articulated device is presented in this work. This hand-made, wooden device is made combining the coil windings of an array of three single transducers. Taking advantage of the sea waves sway, a linear oscillating motion is produced in each transducer generating an electric pulse. Magnetic fundamentals are used to deduce the electrical model of a single transducer, a solenoid-magnet device, and after the model of the whole harvesting array. The energy obtained is stored in a battery and is used to supply a stand-alone system pay-load, for instance a telecom relay or weather station. To maximize the harvested energy, an impedance matching circuit between the generator array and the system battery is required. Two dc-to-dc converters, a buck-boost hybrid cell and a Sepic converter are proposed as impedance adaptors. To achieve this purpose, sliding mode control laws are introduced to impose a loss free resistor behavior to the converters. Although some converters operating at discontinuous conduction mode, like the buck-boost converter, can exhibit also this loss free resistor behavior, they usually require a small input voltage variation range. By means of sliding mode control the loss free resistor behavior can be assured for any range of input voltage variation. After the theoretical analysis, several simulation and experimental results to compare both converters performance are given.

Keywords: harvesting; inductive transducer; sliding mode control; loss free resistor; dc-to-dc converter

1. Introduction

Modern technology consumes large amounts of electrical energy. This energy is usually generated in power plants where different energy sources are converted into electrical energy. Each power plant type and energy source have their own advantages, drawbacks, and conversion efficiencies, but in addition, many of them raise environmental concerns due to the excess of pollutants produced in the conversion procedure.

Although the energy conversion efficiency of power plants can be improved, the pollution and residues generated cannot always be reduced. In this context, renewable energy sources, as hydro power, wind farms, PV (photovoltaic) plants, and the oceans energy, must be profitable to favor a more sustainable development that is respectful with the natural environment.

Depending on the physical characteristic considered, the oceans and sea waters offer different ways to collect the energy of water in movement, namely: Tides, sea-waves, and marine currents. Each water displacement type requires different technologies and transducers for collecting its energy [1].

Wave energy can be a promising energy source. Indeed, the areas of the world having larger wave energy resources are those subjected to regular wind fluxes. There are different harvesting methods. Linear-oscillating magnetic transducers can be used for direct wave energy conversion to electricity. These transducers are usually made with a coil and a permanent magnet [2].

Sea waves are generated when wind passes over the water surface. As the sea waves propagate slower than the wind speed causing them, the energy is transferred from the wind to the waves. Wind friction on the water surface, and the difference of air pressure between the two wave sides, makes stress on the water, causing the waves growth [3]. Then, generated waves propagate on the sea surface, and transport their energy to the shore with the group velocity c_{wg} [4].

The oscillatory motion is higher at the sea surface, and decreases exponentially with depth, making the waves more independent of sea floor contour conditions as the sea depth increases. For this reason, floating harvesters are more competitive than bottom standing ones. Besides, the available energy is higher in near-shore and off-shore locations than in on-shore placements. Figure 1 depicts possible placements for floating harvesting devices.

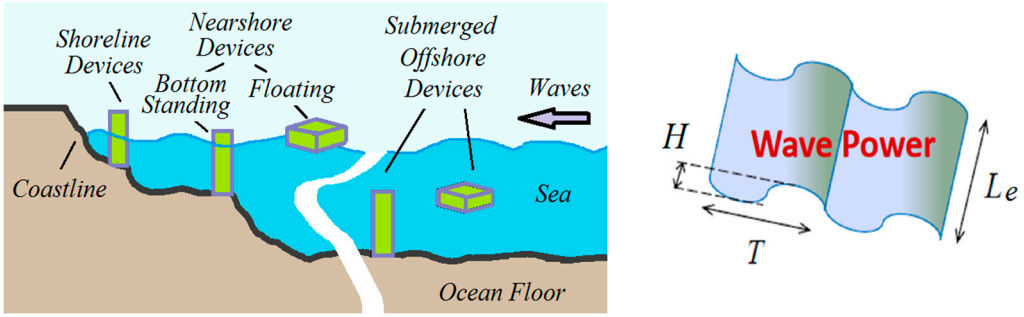

(**a**) (**b**)

Figure 1. Wave-energy harvesting placements, and wave parameters: (**a**) possible harvesting locations and (**b**) marine wave scheme.

The wave height H is given by the wind speed, the sea depth, the fetch angle, and the seafloor topography. The average energy density $d_s[E_w]$ per unit area (1) is the sum of the kinetic and potential energy of the wave [3], where ρ is the density of sea water, H is the wave height, and g is the acceleration of gravitational force. According to the equipartition theorem, both energy types contribute equally to the wave energy. Parameter k_w accounts for the wave periodicity level. Thus, $k_w = 1$ for random waves, and $k_w = 2$ for periodic ones.

$$E_W = E_K + E_P \rightarrow d_S[E_W] = \frac{k_w}{16}\rho g H^2 \ \ [\text{Joule/m}^2] \tag{1}$$

The energy flux, per unit-width, through a vertical plane that is perpendicular to the wave propagation direction is the average power density (2) per unit-width $d_l[P_w]$. Then, the average power available $P_w(L_e)$ in a wave-train with T period and L_e width, can be accounted for with (3). As an example, in a wave train of $H = 1$ m, with a period of $T = 10$ s, the power density is around 5 kW/m.

$$d_l[P_w] = c_{wg} \cdot d_s[E_w] = \frac{k_w c_{wg}}{16}\rho g H^2 \ \ [W/m] \tag{2}$$

$$P_w(L_e) = \frac{k_w \rho g^2}{64\pi} T L_e H^2 \ \ [W], \quad where\ c_{wg} \approx \frac{g}{4\pi} T \tag{3}$$

Notice that although wave parameters $\{T, L_e, H\}$ determine the available wave energy, the real electric power extracted from the sea will depend additionally on the transducer kind, rating, and conversion efficiency, and finally on the efficiency of the power processing circuits used.

Most systems converting wave energy into longitudinal or angular mechanical energy use the upward and downward movement of the waves at a fixed sea point. Thus, in [4–6] electricity is produced by an angular movement using a pulley and a rod to convert a longitudinal movement into an angular one. In this sense, different floating buoys with its respective efficiencies are given in [7].

A difficulty with extracting energy from inductive magnetic energy harvesters is that they normally produce a low AC voltage magnitude at a very low frequency (<10 Hz), and boost transformers cannot be directly used because of their large size. To step-up the voltage many applications propose using a step-up converter after the rectifying stage. Thus, to maximize the harvested energy, the rectifier losses must be reduced. Some literature works propose using voltage multipliers [8], others propose reducing the rectifier voltage drop using mosfet active rectifiers [9,10] as depicted in Figure 2a. The use of two equal generators in counter-phase connected to a three-wire, two-diode full-wave rectifier, has also been proposed in several works, for example in [11,12], and depicted in Figure 2b.

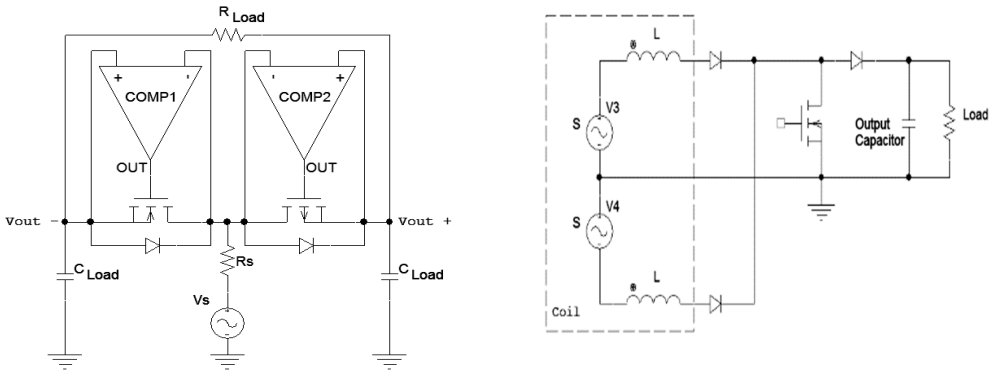

(**a**) (**b**)

Figure 2. Rectifying circuits for inductive harvesting devices: (**a**) active rectifier [9–11] and (**b**) two-generators full-wave rectifier [11–13].

The harvesting device presented here, shown in Figure 3, is made with three inductive transducers with a high output voltage peak. As this device delivers a high voltage output, in clear contrast with previous works, no special rectifier circuits are required. Nevertheless, to reduce the rectifier losses, Schottky diodes have been considered for the full bridge rectifier input stage. Indeed, instead of maximizing the device output voltage combining the three transducer coils in series, a different interconnection has been preferred to reduce the device output impedance, as explained in Section 3.

Impedance matching has been proposed in different works to maximize the energy transfer between the harvesting generator and the load. References [13–18] propose the use of a buck-boost power converter operating in discontinuous conduction mode (DCM) as an impedance adaptor, some of them without voltage sensors [13–15] because input and output adaptor voltages are quite constant; or including voltage feedback to compensate the generator voltage variations [15–17]. Nevertheless, none of them use a harvesting generator with a similar degree of generator voltage variation as proposed in this work. We propose the use of a sliding-mode control to force a switching converter to behave like a loss free resistor (*LFR*) [19] for the impedance adaptor. The inherent robustness to parametric variations of sliding control, can assure a good impedance matching for a wide range of input voltage variation voltage as here.

After this introduction, this work continues as follows. In Section 2, the operation of the harvesting device presented in this work is analyzed, modelled, and verified experimentally. The principle of using an impedance matching circuit to maximize the collected energy is described in Section 3. Next, two sliding mode control laws are proposed to force two different switching converters to behave like a *LFR*-based impedance adaptors. The first converter, the hybrid buck-boost (HBB) is analyzed in Section 4, and next, the Sepic converter is studied in Section 5. The realization of both converters is

described in Section 6. Section 7 is dedicated to the experimental results, and finally in Section 8, some conclusions and future research lines, are given.

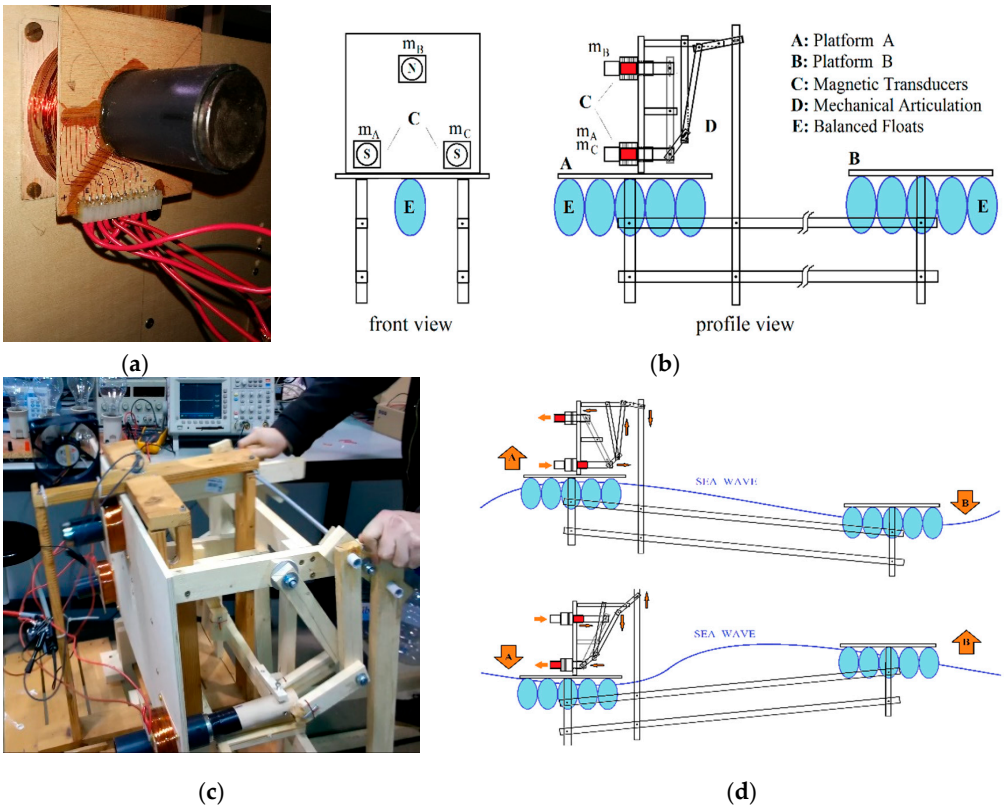

Figure 3. Prototype of a wooden articulated harvesting device made with three transducers: (**a**) detail of a single transducer, (**b**) device scheme: Front and profile views, (**c**) device photograph, and (**d**) operation principle.

2. Transducer and Harvesting Device Description

In this work we propose to use this wave energy for small-power, stand-alone applications. The extraction of small amounts of energy from each wave, conveniently stored in a battery, is a solution to supply intermittent operation small equipment, where the peak power consumption is occasional and brief: Weather stations, telecom relays, and similar equipment.

Figure 3c shows the wooden hand-made, articulated harvesting device, developed in our laboratory. This device includes three magnet-coil transducers (mA, mB, and mC). Figure 3a is depicts one of these transducers. To understand the operation of the real harvesting device appearing in Figure 3c, Figure 3b depicts in a simplified way, the front and profile views of the whole generator, and Figure 3d shows schematically the interaction between the sea waves and the developed generator. To track appropriately the train waves, the balloon floats must have a given amount of water inside, as the floats must only compensate the device weight.

Most harvesting systems that convert wave energy into a longitudinal displacement to drive a coil-magnet based linear generator, use the upward and downward movement of the wave at a fixed point [11,19]. In contrast, the system presented in Figure 3, uses the differential movement between two points of the water surface.

By means of levers, the differential movement caused by a sea wave propagating over the sea is converted into a synchronized horizontal displacement of each magnet through the corresponding coil, inducing a given voltage pulse according to Faraday's law. As seen in Figure 3b,d, the transducer mB is moving in counterphase compared to mA and mC, that are moving in phase. This can be compensated

electrically by modifying the coils connections, or placing two magnets facing a given magnetic pole, and the remaining magnet, to the opposite one."

2.1. Harvesting Transducer Operation Principle

The transducer shown in photograph Figure 3a, a permanent magnet linear generator [20], is depicted schematically in Figure 4. According to its operation principle, a permanent magnet is moving inside and outside of a transducer coil winding. This causes a magnetic flux variation through it, that considering the Faraday's Law, creates a voltage difference across its terminals.

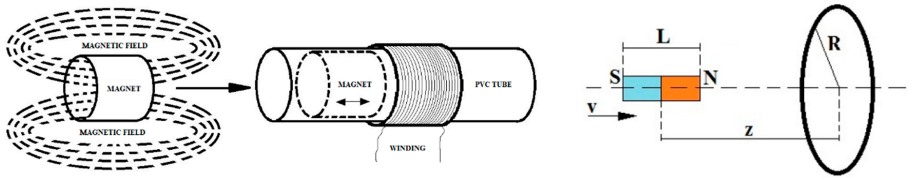

(**a**) (**b**)

Figure 4. Transducer principle operation and description: (**a**) N-turns coil with a moving magnet inside and (**b**) equivalent scheme of the magnet-coil with a single-turn coil carrying N-times the real coil current.

The N-turns coil in Figure 4a, has been idealized in the equivalent diagram of Figure 4b, where all the turns are collapsed in a single turn, of zero thickness and radius R. To produce electricity a magnet of length L, crosses the coil at a variable speed $v(t)$. The distance from the magnet center to the coil center is the variable z. The magnet is modeled as two fictitious magnetic charges of equal value and opposite sign, realizing a magnetic dipole, with both charges separated by the distance L, the magnet length. This approach shown in Figure 5, is sufficient for our purposes.

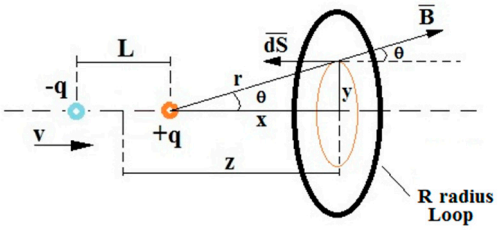

Figure 5. Transducer scheme using the magnetic dipole.

Considering the magnet length L, and its dipolar moment m, the equivalent magnetic charges are $q = \pm m/L$, and the magnetic flux density $B_q(z)$ in the vicinity of a magnetic charge/pole is

$$\vec{B}_q = \frac{\mu_o q}{4\pi r^2}\hat{r} \;\Rightarrow B_q(z) = \frac{\mu_o m}{4\pi L r^2} \tag{4}$$

The total magnetic field $B(z)$ created by both model charges at a given point of the permanent magnet axis placed at a distance z from its center (5), is the sum of contributions of both charges.

$$B(z) = B_{+q} + B_{-q} = \frac{\mu_o m}{4\pi L}\left[\left(z - \frac{L}{2}\right)^{-2} - \left(z + \frac{L}{2}\right)^{-2}\right] \tag{5}$$

The electromagnetic force (EMF) generated by the transducer can be calculated from the total magnetic flux φ created by the dipole charges $\pm q$ through the equivalent collapsed loop.

$$\Phi(z) = \int_S B \cdot d\vec{S} = -\int_S B \cdot dS\cos(\theta) = \Phi_{+q}(z) + \Phi_{-q}(z) \tag{6}$$

$$\Phi_{+q}(z) = -\mathrm{sgn}\left(z - \frac{L}{2}\right)\frac{\mu_o q N}{2}\left\{1 - \left|z - \frac{L}{2}\right| \cdot \left[\left(z - \frac{L}{2}\right)^2 + R^2\right]^{-1/2}\right\} \quad (7)$$

$$\Phi_{-q}(z) = \mathrm{sgn}\left(z + \frac{L}{2}\right)\frac{\mu_o q N}{2}\left\{1 - \left|z + \frac{L}{2}\right| \cdot \left[\left(z + \frac{L}{2}\right)^2 + R^2\right]^{-1/2}\right\} \quad (8)$$

This flux φ is variable because the magnet position z in respect to the coil is changing because the magnet is moving with a certain speed $v(t)$, along the axis spire. Applying Faraday's law to the whole flux produced (6), the EMF induced $\varepsilon(t)$ in the spire is given by (9), where the charges values $\pm q$ have been changed by their equivalent value in terms of the magnetic dipolar moment ($\pm m/L$). When the transducer is placed in a vertical position, the velocity v(t) and the position $z(t)$ are the result of gravitational acceleration, and the potential $\varepsilon(t)$ becomes (10)

$$\varepsilon(t) = -\frac{d\Phi}{dt} = \frac{v(t)N\mu_o m R^2}{2L}v(t) \cdot \left(\left[\left(z(t) - \frac{L}{2}\right)^2 + R^2\right]^{\frac{-3}{2}} - \left[\left(z(t) + \frac{L}{2}\right)^2 + R^2\right]^{\frac{-3}{2}}\right) \quad (9)$$

$$\varepsilon(t) = \frac{gtN\mu_o m R^2}{2L}\left(\left[\left(\frac{gt^2}{2} - \frac{L}{2}\right)^2 + R^2\right]^{\frac{-3}{2}} - \left[\left(\frac{gt^2}{2} + \frac{L}{2}\right)^2 + R^2\right]^{\frac{-3}{2}}\right) \quad (10)$$

The theoretical voltage waveform ε (t) given by expression (10) is shown in Figure 6a, and the real transducer voltage at no-load conditions is given in Figure 6b. The magnet parameters are R = 2.5 cm, L = 6 cm, m = 5.15·10^{-4} Am^2, and the coil has N = 7000 turns of a copper wire with a diameter of φ = 0.3 mm. The measured inductance and resistance are respectively L_T = 3 H and R_T = 424 Ω.

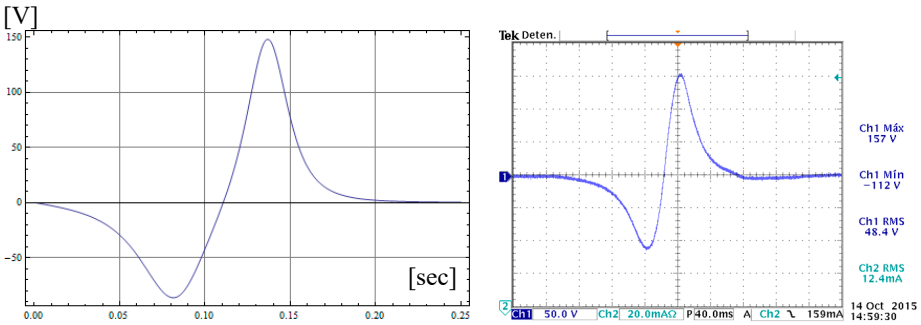

(a) (b)

Figure 6. Pulse voltage generated by the inductive transducer: (**a**) theoretical case and (**b**) real case.

The experimental pulse waveform shown in Figure 6b corresponds to a single transducer with all the partial coil windings are connected in series, and therefore N = 7000 turns. These 7000 turns are organized in five partial windings, three of 1000 turns, and two of 2000 turns. These windings are organized as described in Table 1. Realize that the resistance and inductance of each partial winding (at equal number of turns) is smaller in the inner windings than in the outer ones.

Table 1. Winding parameters of the coil of a single n-transducer, n = {a, b, c}.

Winding	Winding Name	Winding Terminals	Turns	Resistance (Ω)	Inductance (mH)
1st	L1n	1n–2n	1000	43	50
2nd	L2n	3n–4n	2000	104	250
3rd	L3n	5n–6n	1000	61	85
4th	L4n	7n–8n	2000	138	390
5th	L5n	9n–10n	1000	78	120
full coil	L_T	1n–10n	7000	434	3000

2.2. Final Harvesting Device

The harvesting device has three interconnected single transducers. The connections realized between the different windings and coils are given in Figure 7. The final goal is to reduce the device output impedance, increasing also the energy yield.

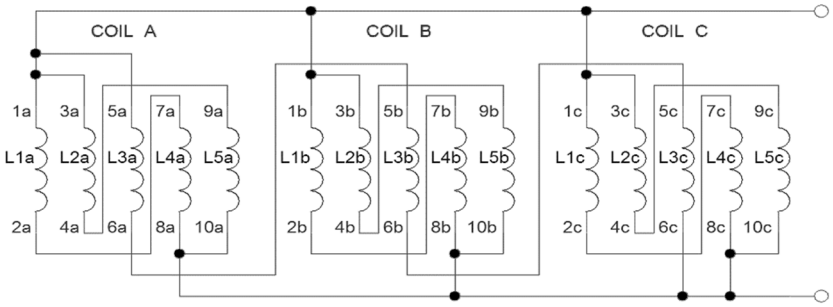

Figure 7. Final harvesting device, and scheme of the array.

According to the circuit of Figure 7, the specific details of the coil-interconnection parameters are given in Table 2.

Table 2. Final Harvesting Device Parameters.

From Coil	Windings Association	Resistance (Ω)	Inductance (mH)
A	W_A = (L1a + L4a) || (L2a + L5a)	91.15	200
B	W_B = (L1b + L4b) || (L2b + L5b)	91.15	200
C	W_C = (L1c + L4c) || (L2c + L5c)	91.15	200
A, B, C	W_D = L3a + L3b + L3c	183.3	255
device	W_A || W_B || W_C || W_D	26.06	52.86

At no-load conditions, the voltage pulse produced by the proposed device is shown in Figure 8. The final parameters of this generator are: R_{int} = 26 Ω, L_{int} = 52.8 mH.

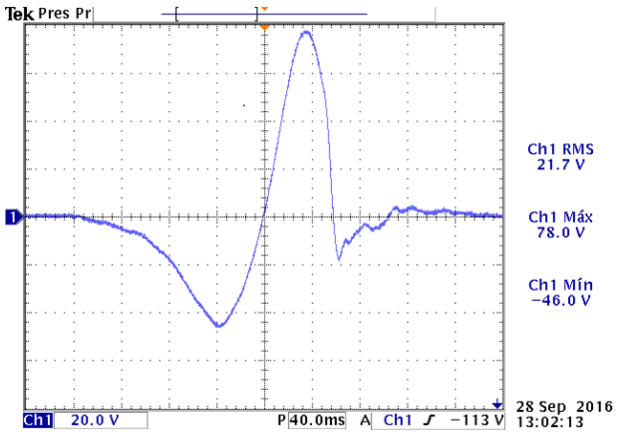

Figure 8. Experimental pulse voltage of the harvesting. Device/generator at no-load condition.

3. Impedance Matching with a Loss Free Resistor

The main purpose of the work presented here is to charge the pay-load system battery taking as much as energy as possible from the harvesting generator. If the battery is connected directly to the generator, using only a bridge rectifier, the transferred energy cannot be maximized, in part due to impedance mismatching between the battery and the generator, and in addition, because only the

parts of the input voltage pulse waveform exceeding the battery voltage will be profited. Figure 9 depicts the proposed solution, a matching circuit between the generator and the battery.

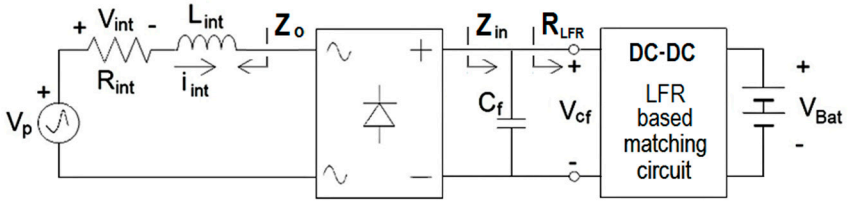

Figure 9. Proposed matching idea using the generator equivalent circuit.

Therefore, the impedance adaptation is the only solution to maximize the energy transferred at any working condition. However, even in this case, only 50% of the energy produced in the transducer will be transferred to the load. Indeed, if the conjugate input impedance of the power adaptor were equal to the generator output impedance (11), a perfect adaptation would occur.

For its simplicity, a DC-DC converter behaving as a loss free resistor [21] is proposed as impedance matching circuit. The *LFR* is a two-port circuit with a resistive input impedance R_{LFR} that can be adjusted. The output port, with a power source characteristic, delivers to the load, in this case the system battery, all the power absorbed by the *LFR* input resistance.

$$\left.\begin{array}{c} Z_o = R_{\text{int}} + j\omega L_{\text{int}} = 26 + j0.33\ [\Omega] \\ Z_{in}^{*} = \left(R_{LFR} \parallel \frac{-j}{\omega\, C_f}\right)^{*} = \frac{jR_{LFR}/\omega\, C_f}{R_{LFR}+j/\omega\, C_f} = 25.96 + j0.045\ [\Omega] \end{array}\right\} \textit{then}\ Z_o = Z_{in}^{*} \Leftrightarrow R_{\text{int}} \approx R_{LFR} \qquad (11)$$

Expression (11) shows the generator output impedance Z_o, and Z^*_{in}, that is the conjugate of the matching circuit input impedance. The numerical values for Z_o and Z^*_{in} appearing in (11) have been calculated for C_f = 10 μF, and considering the worst case shown in Table 3. This means a time lapse between consecutive waves of one second (ΔT = 1 s), although the real one is longer, between 10 and 30 seconds."

Table 3. Real and imaginary parts of Z_o and Z^*_{in} for C_f = 10 μF, and different lapse times ΔT between waves.

[Ω]	∞	30 s	10 s	3 s	1 s
Re [Z_o]	26	26	26	26	26
Re [Z^*_{in}]	R_{LFR}	R_{LFR}	R_{LFR}	R_{LFR}	R_{LFR}
Im [Z_o]	0	10^{-2}	$3.3{\cdot}10^{-2}$	10^{-1}	0.33
Im [Z^*_{in}]	0	$1.5{\cdot}10^{-3}$	$4.5{\cdot}10^{-3}$	$1.5{\cdot}10^{-2}$	$4.5{\cdot}10^{-2}$

The design of filter capacitor C_f implies three different concerns: (a) the low-pass filter effect must be small because its voltage $v_{cf}(t)$ must track appropriately the generator pulses $v_p(t)$, (b) the capacitor must compensate the inductive impedance of the generator, and (c) the capacitor must filter the high frequency switching noise. Finally, the selected value for the capacitor is C_f = 10 μF.

According to circuit of Figure 8, the instantaneous capacitor voltage $v_{cf}(t)$ is given in (12). Next, neglecting the rectifier bridge voltage drop $2V_d$, and assuming impedance matching (R_{LFR} = 26 Ω), the capacitor voltage $v_{cf}(t)$ should be (13) the half of the input pulse absolute value.

$$v_{Cf}(t) \approx \left|v_p(t) - R_{\text{int}} I_{\text{int}}(t) - 2V_d\right| \qquad (12)$$

$$v_{Cf}(t) \approx \left|v_{\text{int}}(t)\right| = \frac{\left|v_p(t)\right|}{2} \qquad (13)$$

The *LFR* behavior is required for impedance matching, but the appropriate converter to implement the *LFR* depends on its input and output voltage ranges.

According to the pulse waveform in Figure 7, the capacitor voltage v_{Cf}(t) experiences a large variation following the voltage pulse v_p evolution. During 250 ms, the generator voltage varies from $-100\text{ V} < v_p(t) < 160\text{ V}$. Once rectified, if impedance matching occurs, the capacitor voltage changes from $0 < v_{Cf}(t) < V_{max} = 80\text{ V}$. Thus, using a common 12 V battery, the matching circuit input voltage $v_{Cf}(t)$ can be greater ($v_{Cf}(t) > V_{bat}$) or smaller ($v_{Cf}(t) < V_{bat}$) than the battery voltage. Consequently, any converter proposed as matching circuit must exhibit a buck-boost characteristic.

3.1. DCM Operated Buck-Boost Converter

Since the buck-boost operated at DCM [19] has a natural *LFR* behavior, that converter could be proposed as an impedance matching circuit. From the buck-boost input power in DCM, the expression of the converter input impedance R_{LFR} can be easily calculated (14)

$$P_{in} = \frac{v_{cf}^2 D^2 T_S}{2L} = \frac{v_{cf}^2}{R_{LFR}} \Rightarrow R_{LFR} = \frac{2L}{D^2(t)T_S(t)} \approx R_{\text{int}} = 26\,\Omega \tag{14}$$

where D is the converter duty ratio, and T_S is the switching period. Theoretically, any pair of constant D and T_S can be used to regulate the input impedance $R_{LFR} = 26\ \Omega$. However, to guarantee that the converter is working in the discontinuous mode, the converter duty ratio $D(t)$ must change continuously (15) to follow the $v_{Cf}(t)$. Therefore, to keep constant, at 26 Ω, the switching frequency $f_S(t) = 1/T_S(t)$ must also be adapted continuously.

$$\left.\begin{array}{c}\text{DCM} \\ < v_L >= 0\end{array}\right\} \Rightarrow D(t) < \frac{V_{bat}}{V_{bat} + v_{Cf}(t)} \tag{15}$$

It can be easily concluded that designing a low consumption control circuit able to adjust continuously the values of duty cycle $D(t)$ and T_S (t) to fulfill simultaneously nonlinear Equation (14) and in Equation (15) is very complicated. Besides, the buck-boost converter has output voltage sign inversion, input and output pulsating currents, and, therefore, other solutions must be explored.

3.2. Buck/Boost Hybrid Converter (HBB)

The buck/boost hybrid converter is shown in Figure 10. While $v_{Cf}(t)$ be smaller than the battery voltage V_{bat}, the circuit will operate in boost mode, but when $v_{Cf}(t)$ be greater than the battery one, it will work in buck mode. When the converter is in step-up mode, S_{Buck} is permanently at ON-state, whereas in the buck working mode S_{Boost} is permanently at OFF-state.

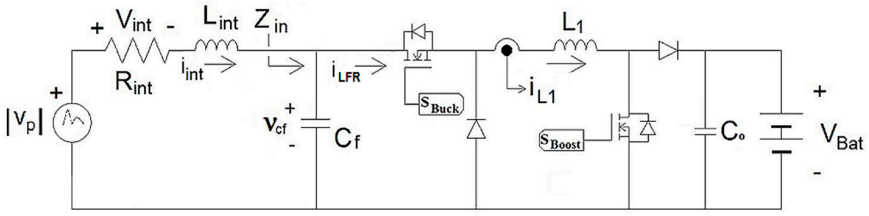

Figure 10. Buck/Boost Hybrid Converter (HBB).

This converter has a pulsating output current in boost mode and a pulsating input current in buck mode, so there is an electromagnetic interference (EMI) reduction.

To impose a *LFR* behavior to both working modes, assuring impedance matching, two sliding control laws must be used, one per each mode. Both control surfaces are analyzed in Section 4.

The mode selection is done with a comparator, but there is a small dead-zone around V_{bat} where the converter is not switching to reduce switching losses. This is an advantage compared to a classic step-up/down converter like the buck-boost, Ćuk, or Sepic, that are switching continuously regardless the value of $v_{Cf}(t)$ and V_{bat}. Conversely, in the dead zone, there is no control, and the impedance matching is lost.

3.3. Sepic Converter

Figure 11 depicts the Sepic converter. As in the HBB converter case, there is no output voltage sign change. As happens with the HBB converter in the boost mode, the input current has a triangular waveform whereas the output current is pulsating. In this case, as there is no dead-zone around V_{bat}, the impedance matching occurs for any $v_{cf}(t)$ value. Besides, as additional advantage, only one sliding-mode control law is required to impose the *LFR* behavior for all $v_{cf}(t)$ voltage range.

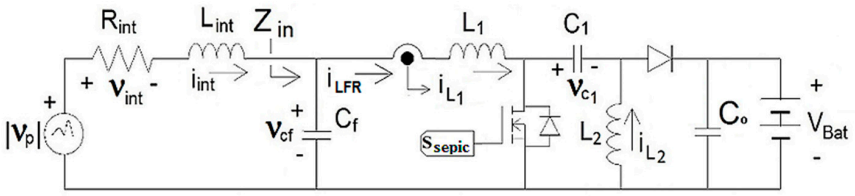

Figure 11. Sepic Converter.

4. HBB Converter Matching Circuit

The hybrid converter is a combination of two converters. Therefore, it has two operation modes, buck and boost. Two different sliding mode surfaces are required to force this circuit to behave like a loss free resistor. The controllable inductor is L_1. In the boost mode, the inductor current $i_{L1}(t)$ is the converter input current, so $i_{L1}(t) = i_{LFR}(t)$. Conversely, in the buck mode, $i_{L1}(t)$ is the converter output current, that is, the current charging the battery, and therefore $i_{LFR}(t) = i_{L1}(t) \cdot [V_{bat}(t)/v_{cf}(t)]$.

4.1. Boost Mode Operation (HBB)

When $v_{Cf}(t) < V_{bat}$, the switch S_{Buck} is always at ON state, and $i_{L1}(t) = i_{int}(t)$. The resulting circuit is an input filtered boost converter. The output capacitor C_o is not included because it is in parallel with the battery and has no dynamics. For simplicity, we use $v_p(t)$ in the analysis, instead of $|v_p(t)|$. Figure 12 depicts the two circuit topologies, ON and OFF.

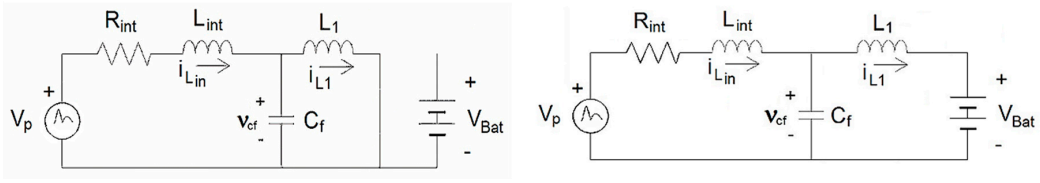

Figure 12. Boost mode, HBB converter topologies: (**a**) ON and (**b**) OFF.

Using the switching variable $u(t) = \{0, 1\}$ the equations of ON and OFF topologies can be compacted, and the converter dynamics at any instant is described with a sole set of Equations, (16)

$$x(t) = \begin{bmatrix} i_{int} \\ i_{L1} \\ v_{cf} \end{bmatrix} \Rightarrow \begin{cases} L_{int}\frac{di_{int}}{dt} = v_P - R_{int}i_{int} - v_{cf} \\ L_1\frac{di_{L_1}}{dt} = v_{cf} - V_{Bat}(1-u) \\ C_f\frac{dv_{cf}}{dt} = i_{int} - i_{L1} \end{cases} \quad (16)$$

The sliding surface (17) imposed to the inductor current $i_{L1}(t)$, guarantees the impedance matching. From the Equation set (16), taking into account the control surface $S(x)$ and its existence conditions, the equivalent control (18) is obtained.

$$S(x) = i_{L1} - \frac{v_{cf}}{R_{int}} = 0 \Rightarrow i_{LFR} = \frac{v_{cf}}{R_{int}} \; S(x)\dot{S}(x) < 0 \tag{17}$$

$$u_{eq} = 1 - \frac{v_{cf}}{V_{Bat}} + \frac{L_1}{R_{int} V_{Bat}} \cdot \frac{dv_{cf}}{dt} \tag{18}$$

Forcing to zero the dynamics of Equation set (16), and considering the equivalent control (18), the system equilibrium point (19) and the related ideal sliding dynamics (20) can be obtained. The resulting dynamics is linear. At the equilibrium point, the capacitor voltage results to be the half part of the input voltage pulse ($V_{cf}^{*} = V_p^{*}/2$), as expected from an impedance matching system.

$$X^{*} = \left[I_{int}^{*}, V_{cf}^{*}, I_{L_1}^{*}\right]^T = \left[\frac{V_P^{*}}{2R_{int}}, \frac{V_P^{*}}{2}, \frac{V_P^{*}}{2R_{int}}\right]^T \tag{19}$$

$$\begin{cases} g_1(x) = \frac{di_{int}}{dt} = \frac{1}{L_{\text{int}}} v_P - \frac{R_{int}}{L_{int}} i_{\text{int}} - \frac{1}{L_{int}} v_{cf} \\ g_2(x) = \frac{dv_{cf}}{dt} = \frac{1}{C_f} i_{int} - \frac{v_{cf}}{R_{int} C_f} \end{cases} \tag{20}$$

The ideal sliding dynamics is linear, as can be seen in (20). Consequently, the Laplace transform can be directly applied in the ideal dynamics (20), and a small signal model is not required. After some manipulations the transfer function $V_{cf}(s)/V_p(s)$ (21) is obtained. This transfer function evidences the impedances matching at DC, because $V_{Cf}/V_p = 1/2$. The tracking of the input pulse $v_p(t)$ is controlled by a second order low-pass filter, with a characteristic polynomial $P(s)$ is unconditionally stable, because all its coefficients exist and are positive. Considering that $C_f = 10$ µF, the system natural frequency (21) is $\omega_n \approx 1900$ rad/s, and the bandwidth is around BW_{-3dB}–310 Hz.

$$\frac{V_{cf}(s)}{V_P(s)} = \frac{\hat{V}_{cf}(s)}{\hat{V}_P(s)} = \frac{K}{P(s)} = \frac{\frac{1}{L_{in} C_f}}{s^2 + \left(\frac{R_{in}}{L_{in}} + \frac{1}{R_{in} C_f}\right) s + \frac{2}{L_{in} C_f}} \tag{21}$$

4.2. Buck Mode Operation (HBB)

When $v_{Cf}(t) < V_{bat}$, the switch S_{Boost} will be permanently at OFF state. The resulting circuit is a common buck converter with an input filter. The output capacitor C_o is not depicted because is in parallel with the battery. The topologies ON and OFF, are shown respectively in Figure 13a,b.

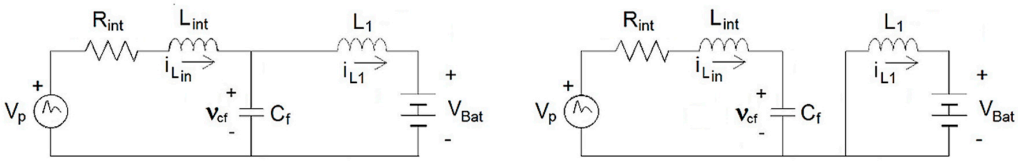

(**a**) (**b**)

Figure 13. Buck mode, HBB converter topologies: (**a**) ON, (**b**) OFF.

Repeating the process described for the boost mode, a single set of differential Equation (22) describes, at any instant, the dynamics of the converter.

$$x(t) = \begin{bmatrix} i_{\text{int}} \\ i_{L1} \\ v_{cf} \end{bmatrix} \Rightarrow \begin{cases} L_{int}\frac{di_{int}}{dt} = v_P - R_{int}i_{int} - v_{cf} \\ L_1\frac{di_{L_1}}{dt} = v_{cf}\,u - V_{Bat} \\ C_f\frac{dv_{cf}}{dt} = i_{int} - i_{L1}\,u \end{cases} \tag{22}$$

To assure impedance matching, the converter input current should be forced to be proportional to the input voltage $v_{Cf}(t)$. However, the only state variable leading to a stable control surface is the output current $i_{L1}(t)$. As a result, the proposed sliding surface (23) regulates the output current $i_{L1}(t)$ to a given value that, considering the converter voltage gain, imply the desired input current, that is $i_{LFR}(t)$. From the Equation set (22), considering the surface $S(x)$ and its existence conditions, the equivalent control (24) is obtained.

$$S(x) = i_{L1} - \frac{v_{cf}}{R_{int}} \cdot \frac{v_{cf}}{V_{Bat}} = 0 \;\Rightarrow\; i_{LFR} = \frac{v_{cf}}{R_{int}} \;\; S(x)\dot{S}(x) < 0 \tag{23}$$

$$u_{eq} = 1 - \frac{v_{cf}}{V_{Bat}} + \frac{L_1}{R_{int}V_{Bat}} \cdot \frac{dv_{cf}}{dt} \tag{24}$$

Forcing to zero the system dynamics in (22), and considering the equivalent control (24), we obtain the equilibrium point (25) and the corresponding ideal sliding dynamics (26), that is non-linear. As happened in the boost mode, the equilibrium point capacitor voltage is the half part of the pulse voltage is ($V^*_{\text{cf}} = V^*_p/2$), as expected from impedance matching.

$$X^* = \left[I^*_{in}, V^*_{cf}, I^*_{L_1}\right]^T = \left[\frac{V_P{}^*}{2R_{\text{int}}}, \frac{V_P{}^*}{2}, \frac{V^{*2}_{cf}}{4R_{int}V_{Bat}}\right]^T \tag{25}$$

$$\begin{cases} g_1(x) = \frac{di_{int}}{dt} = \frac{1}{L_{int}}v_P - \frac{R_{int}}{L_{int}}i_{\text{int}} - \frac{1}{L_{int}}v_{cf} \\ g_2(x) = \frac{di_{L1}}{dt} = \frac{2v_{cf}}{R_{int}V_{Bat}} \cdot \frac{dv_{cf}}{dt} \\ g_3(x) = \frac{dv_{cf}}{dt} = \frac{1}{C_f}i_{int} - \frac{2}{C_f}\frac{L_1}{R_{int}V_{Bat}}\frac{dv_{cf}}{dt}i_{L1} - \frac{V_{Bat}}{v_{cf}}\frac{i_{L1}}{C_f} \end{cases} \tag{26}$$

To evaluate the local stability, the ideal dynamics (26) is linearized around the equilibrium point X^* using the typical small signal perturbation model (27), (28), whose coefficients are given in (29)

$$x(t) = X^* + \hat{x}(t) \tag{27}$$

$$\begin{cases} g_1(x) \approx \boldsymbol{a}\cdot\hat{v}_P(t) + \boldsymbol{b}\cdot\hat{i}_{int}(t) + \boldsymbol{c}\cdot\hat{v}_{cf}(t) \\ g_2(x) \approx \boldsymbol{d}\cdot\hat{v}_{cf}(t) + \boldsymbol{e}\cdot\hat{w}(t) \; where \; w = \frac{dv_{cf}}{dt} \qquad , \; W^* = 0 \\ g_3(x) \approx \boldsymbol{f}\cdot\hat{i}_{int}(t) + \boldsymbol{g}\cdot\hat{i}_{L1}(t) + \boldsymbol{h}\cdot\hat{v}_{cf}(t) + \boldsymbol{k}\cdot\hat{w}(t) \end{cases} \tag{28}$$

$$\begin{array}{lll} \boldsymbol{a} = \left.\frac{\partial g_1}{\partial v_P}\right|_{x^*} = \frac{1}{L_{in}} & \boldsymbol{b} = \left.\frac{\partial g_1}{\partial i_{int}}\right|_{x^*} = -\frac{R_{int}}{L_{in}} & \boldsymbol{c} = \left.\frac{\partial g_1}{\partial v_{cf}}\right|_{x^*} = -\frac{1}{L_{in}} \\ \boldsymbol{d} = \left.\frac{\partial g_2}{\partial v_{cf}}\right|_{x^*} = 0 & \boldsymbol{e} = \left.\frac{\partial g_2}{\partial w}\right|_{x^*} = \frac{V^*_P}{R_{int}V_{Bat}} & \boldsymbol{f} = \left.\frac{\partial g_3}{\partial i_{int}}\right|_{x^*} = \frac{1}{C_f} \\ \boldsymbol{g} = \left.\frac{\partial g_3}{\partial i_{L1}}\right|_{x^*} = \frac{-2V_{Bat}}{V^*_P C_f} & \boldsymbol{h} = \left.\frac{\partial g_3}{\partial v_{cf}}\right|_{x^*} = \frac{1}{R_{int}C_f} & \boldsymbol{k} = \left.\frac{\partial g_3}{\partial w}\right|_{x^*} = \frac{-L_1}{2C_f}\left(\frac{V^*_P}{R_{int}V_{Bat}}\right)^2 \end{array} \tag{29}$$

Applying the Laplace transform to the linearized model (28) with the coefficients of (29), the $\hat{V}_{cf}(s)/\hat{V}_p(s)$ transfer function (30) is obtained. This function evidences the impedance matching at

DC because V_{Cf}/V_p = 1/2. As in the previous case, the tracking of $v_p(t)$ is given by a low-pass filter of second order. The system stability is verified because all coefficients of $P(s)$ exist and are positive.

$$\frac{\hat{V}_{cf}(s)}{\hat{V}_P(s)} = \frac{\frac{1}{L_{int}C_f}}{s^2\left[1+\frac{L_1}{2C_f}\left(\frac{V_P^*}{R_{int}V_{Bat}}\right)^2\right]+s\left\{\frac{1}{R_{int}C_f}\left[1+\frac{L_1}{2L_{int}}\left(\frac{V_P^*}{V_{Bat}}\right)^2\right]+\frac{R_{int}}{L_{int}}\right\}+\frac{2}{L_{int}C_f}} \tag{30}$$

As expected from the nonlinear sliding dynamics (26), in the buck mode, the bandwidth B_{-3d}, and the natural frequency (31) are not constant, depending on the generator pulse V_P and the converter gain. Realize that in the boost mode (18) the natural frequency was constant.

$$\omega_n^2 = \frac{2}{L_{int}C_f}\cdot\left[1+\frac{L_1}{2C_f}\left(\frac{V_P^*}{R_{int}V_{Bat}}\right)^2\right]^{-1} \tag{31}$$

5. Sepic Converter Matching Circuit

In the Sepic converter the controllable inductor is L_1. As in the HBB boost mode, the current through this inductor $i_{L1}(t)$ corresponds to the converter input current $i_{LFR}(t)$. This circumstance allows using the same control surface $S(x)$ to force the *LFR* behavior that was proposed for the HBB boost mode in Section 4. Figure 14 depicts the two converter topologies.

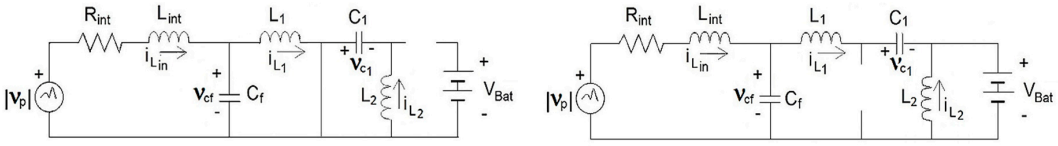

Figure 14. Sepic converter topologies: (**a**) ON and (**b**) OFF.

Again, in the previous cases by means of the switching variable $u(t) = \{0, 1\}$, the dynamics of the converter at any instant can be described with a single set of differential Equation (32).

$$x(t) = \begin{bmatrix} i_{\text{int}} \\ i_{L1} \\ i_{L2} \\ v_{c1} \\ v_{cf} \end{bmatrix} \Rightarrow \begin{cases} L_{int}\frac{di_{int}}{dt} = v_P - R_{int}i_{int} - v_{cf} \\ L_1\frac{di_{L_1}}{dt} = v_{C_f} - (1-u)\left(v_{C_1}+V_{Bat}\right) \\ L_2\frac{di_{L_2}}{dt} = -V_{Bat} + u\left(v_{C_1}+V_{Bat}\right) \\ C_f\frac{dv_{C_f}}{dt} = i_{int} - i_{L_1} \\ C_1\frac{dv_{C_1}}{dt} = i_{L_1} - u\left(i_{L_1}+i_{L_2}\right) \end{cases} \tag{32}$$

The sliding surface (33) imposed to the inductor current $i_{L1}(t)$ assures the impedance matching. The equivalent control (34) is deduced from the Equation set (32), using the surface $S(x)$ and its related existence conditions.

$$S(x) = i_{L1} - \frac{v_{C_f}}{R_{int}} = 0 \;\Rightarrow\; i_{LFR} = \frac{v_{cf}}{R_{int}} \;\; S(x)\dot{S}(x) < 0 \tag{33}$$

$$u_{eq}(t) = 1 - \frac{v_{C_f}}{\left(v_{C_1}+V_{Bat}\right)} + \frac{L_1}{R_{\text{int}}\left(v_{C_1}+V_{Bat}\right)}\cdot\frac{dv_{C_f}}{dt} \tag{34}$$

Forcing to zero the dynamics shown in (32), and considering the equivalent control (34), the equilibrium point (35) and the corresponding ideal dynamics (36) are deduced, which result to be

non-linear. As in boost mode, the capacitor voltage at the equilibrium point is again, the half part of the pulse voltage is ($V_{cf}^{*} = V_{p}^{*}/2$), corresponding to a situation of impedance matching.

$$X^{*} = \left[I_{\text{int}}^{*}, I_{L_1}^{*}, I_{L_2}^{*}, V_{C_f}^{*}, V_{C_1}^{*}\right]^{T} = \left[\frac{V_P^{*}}{2 \cdot R_{\text{int}}}, \frac{V_P^{*}}{2 \cdot R_{\text{int}}}, \frac{V_P^{*\,2}}{4 \cdot R_{\text{int}} V_{Bat}}, \frac{V_P^{*}}{2}, \frac{V_P^{*}}{2}\right]^{T} \tag{35}$$

$$\begin{cases} g_1(x) = \frac{di_{int}}{dt} = \frac{1}{L_{int}}\left[v_P - R_{int} i_{int} - v_{cf}\right] \\ g_2(x) = \frac{di_{L_1}}{dt} = \frac{1}{R_{\text{int}}} \frac{dv_{C_f}}{dt} \\ g_3(x) = \frac{di_{L_2}}{dt} = \frac{1}{L_2}\left[v_{C_1} - v_{C_f} + \frac{L_1}{R_{\text{int}}} \cdot \frac{dv_{C_f}}{dt}\right] \\ g_4(x) = \frac{dv_{C_f}}{dt} = \frac{1}{C_f}\left[i_{int} - i_{L_1}\right] \\ g_5(x) = \frac{dv_{C_1}}{dt} = \frac{1}{C_1}\left\{\frac{i_{L_1}+i_{L_2}}{v_{C_1}+V_{Bat}} \cdot \left[v_{C_f} - \frac{L_1}{R_{\text{int}}} \cdot \frac{dv_{C_f}}{dt}\right] - i_{L_2}\right\} \end{cases} \tag{36}$$

To evaluate the local stability of the proposed surface, the ideal dynamics (32) should be linearized around the equilibrium point X^{*} using the well-known small signal perturbation model (37), (38). The coefficients of the small signal model are given in (39).

$$x(t) = X^{*} + \hat{x}(t) \tag{37}$$

$$\begin{cases} g_1(x) = \frac{di_{int}}{dt} = \boldsymbol{a} \cdot \hat{v}_P(t) + \boldsymbol{b} \cdot \hat{i}_{int}(t) + \boldsymbol{c} \cdot \hat{v}_{cf}(t) \\ g_2(x) = \frac{di_{L_1}}{dt} = \boldsymbol{d} \cdot \hat{w}(t) \; where, w(t) = \frac{dv_{C_f}}{dt} \\ g_3(x) = \frac{di_{L_2}}{dt} = \boldsymbol{e} \cdot \hat{v}_{C_1}(t) + \boldsymbol{f} \cdot \hat{w}(t) + \boldsymbol{h} \cdot \hat{v}_{C_f}(t) \\ g_4(x) = \frac{dv_{C_f}}{dt} = \boldsymbol{j} \cdot \hat{i}_{int}(t) + \boldsymbol{k} \cdot \hat{i}_{L_1}(t) \\ g_5(x) = \frac{dv_{C_1}}{dt} \approx \boldsymbol{m} \cdot \hat{i}_{L_2}(t) + \boldsymbol{n} \cdot \hat{i}_{L_1}(t) + \boldsymbol{p} \cdot \hat{w}(t) + \boldsymbol{q} \cdot \hat{v}_{C_1}(t) + \boldsymbol{r} \cdot \hat{v}_{C_f}(t) \end{cases} \tag{38}$$

$$\begin{cases} \boldsymbol{a} = \left.\frac{\partial g_1}{\partial v_P}\right|_{X^{*}} = \frac{1}{L_{int}} & \boldsymbol{e} = \left.\frac{\partial g_3}{\partial v_{C_1}}\right|_{X^{*}} = \frac{1}{L_2} & \boldsymbol{m} = \left.\frac{\partial g_5}{\partial i_{L_2}}\right|_{X^{*}} = \frac{-2V_{Bat}}{C_1\left(V_P^{*}+2V_{Bat}\right)} & \\ \boldsymbol{b} = \left.\frac{\partial g_1}{\partial i_{int}}\right|_{X^{*}} = \frac{-R_{int}}{L_{int}} & \boldsymbol{f} = \left.\frac{\partial g_3}{\partial w}\right|_{X^{*}} = \frac{L_1}{L_2 R_{\text{int}}} & \boldsymbol{n} = \left.\frac{\partial g_5}{\partial i_{L_1}}\right|_{X^{*}} = \frac{V_P^{*}}{C_1\left(V_P^{*}+2V_{Bat}\right)} & \boldsymbol{k} = \left.\frac{\partial g_4}{\partial i_{L_1}}\right|_{X^{*}} = \frac{-1}{C_f} \\ \boldsymbol{c} = \left.\frac{\partial g_1}{\partial v_{C_f}}\right|_{X^{*}} = \frac{-1}{L_{int}} & \boldsymbol{h} = \left.\frac{\partial g_3}{\partial v_{C_f}}\right|_{X^{*}} = \frac{-1}{L_2} & \boldsymbol{q} = \left.\frac{\partial g_5}{\partial v_{C_1}}\right|_{X^{*}} = \frac{-V_P^{*\,2}}{2R_{\text{int}}C_1 V_{Bat}\left(2V_{Bat}+V_P^{*}\right)} & \boldsymbol{p} = \left.\frac{\partial g_5}{\partial w}\right|_{X^{*}} = \frac{-V_P^{*}}{2C_1 R_{\text{int}}^{2} V_{Bat}} \\ \boldsymbol{d} = \left.\frac{\partial g_2}{\delta w}\right|_{X^{*}} = \frac{1}{R_{\text{int}}} & \boldsymbol{j} = \left.\frac{\partial g_4}{\partial i_{int}}\right|_{X^{*}} = \frac{1}{C_f} & \boldsymbol{r} = \left.\frac{\partial g_5}{\partial v_{C_f}}\right|_{X^{*}} = \frac{V_P^{*}}{2R_{\text{int}}C_1 V_{Bat}} & \end{cases} \tag{39}$$

After linearizing (38) the ideal dynamics, the small signal $\hat{V}_{cf}(s)/\hat{V}_p(s)$ transfer function (40) is obtained, that evidences the perfect impedance matching is at DC, and good at low frequency, like the sea waves-trains. Realize in (40) that at DC $V_{Cf} = 1/2V_p$. When frequency increases the module of $\hat{V}_{cf}(s)/\hat{V}_p(s)$ decreases from its maximum value at DC (1/2) and the phase-shift between V_{Cf} and V_p increases. As in the HBB boost mode, the natural frequency is given by L_{int} and the capacitor C_f.

$$H_{C_f P}(s) = \frac{\hat{V}_{C_f}(s)}{\hat{V}_P(s)} = \frac{1/L_{int}C_f}{s^2 + s\left(\frac{L_{int}+C_f R_{\text{int}}{}^2}{C_f R_{\text{int}} L_{int}}\right) + \frac{2}{L_{int}C_f}} = \frac{1}{2} \cdot \frac{\omega_{na}^2}{s^2 + 2\zeta_a \omega_{na} s + \omega_{na}^2} \tag{40}$$

The Sepic converter is a fifth order system, and the ideal system dynamics should be of fourth order, but expression (40) denotes a second order system. The fourth order dynamics consists of two decoupled pairs of complex conjugated poles that can be factorized in two second order functions as seen in (41). The converter is stable, since all its coefficients of $D_a(s)$ and $D_b(s)$ exist and are positive. In a clear contrast to $H_{CfP}(s)$, where a pair of complex conjugated poles is hidden, in other system transfer functions the whole dynamics are visible. One of these cases is the $H_{C1P}(s)$ transfer function, where

according to expressions (42) and (43), the full dynamics is shown. Realize that s expected, at DC conditions $V_{Cf} = V_{C1}$.

$$P(s) = \left(s^2 + 2\zeta_a\omega_{na}s + \omega_{na}^2\right)\cdot\left(s^2 + 2\zeta_b\omega_{nb}s + \omega_{nb}^2\right) = D_a(s)\cdot D_b(s) \tag{41}$$

$$H_{C_1P}(s) = \frac{\hat{V}_{C_1}(s)}{\hat{V}_P(s)} = \frac{\hat{V}_{C_1}(s)}{\hat{V}_{C_f}(s)}\cdot\frac{\hat{V}_{Cf}(s)}{\hat{V}_P(s)} = H_{C1Cf}(s)\cdot H_{C_fP}(s) \tag{42}$$

$$H_{C1Cf}(s) = \frac{\hat{V}_{C_1}(s)}{\hat{V}_{C_f}(s)} = \frac{-s^2L_2\left(V_P^*+2V_{Bat}\right)+\left[4V_{Bat}^2L_1+2V_P^*L_2V_{Bat}+V_P^*L_2\left(V_P^*+2V_{Bat}\right)\right]R_{\text{int}}\cdot s+4R_{int}^2V_{Bat}^2}{2s^2\left[R_{int}^2L_2C_1V_{Bat}\left(V_P^*+2V_{Bat}\right)\right]+s\cdot R_{\text{int}}L_2V_P^{*2}+4R_{int}^2V_{Bat}^2} \tag{43}$$

6. Experimental Circuits of the Impedance Adaptors

Figures 15 and 16 depict the Sepic converter and its control board, respectively.

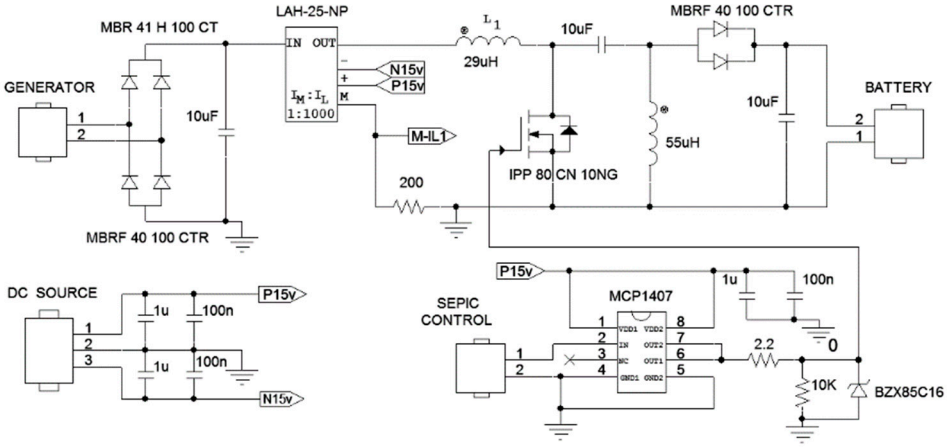

Figure 15. Sepic converter power stage.

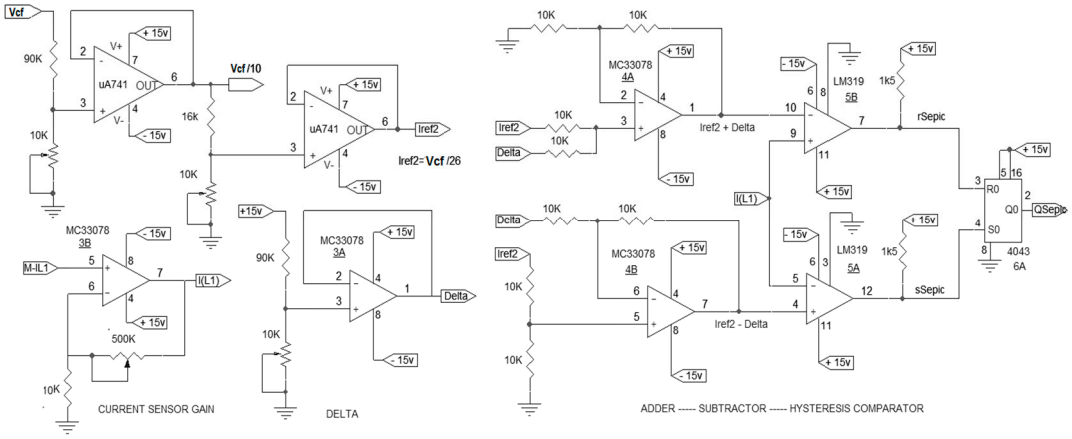

Figure 16. Sepic control board.

Figures 17 and 18 depict the HBB power stage and its control board. The boost mode HBB and the Sepic control circuits mode are equal, because the control surface is the same, see (17) and (33).

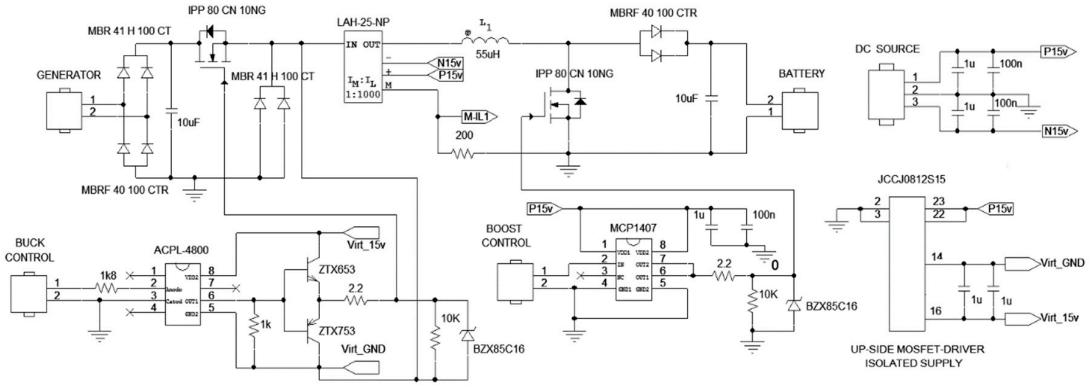

Figure 17. HBB converter power stage.

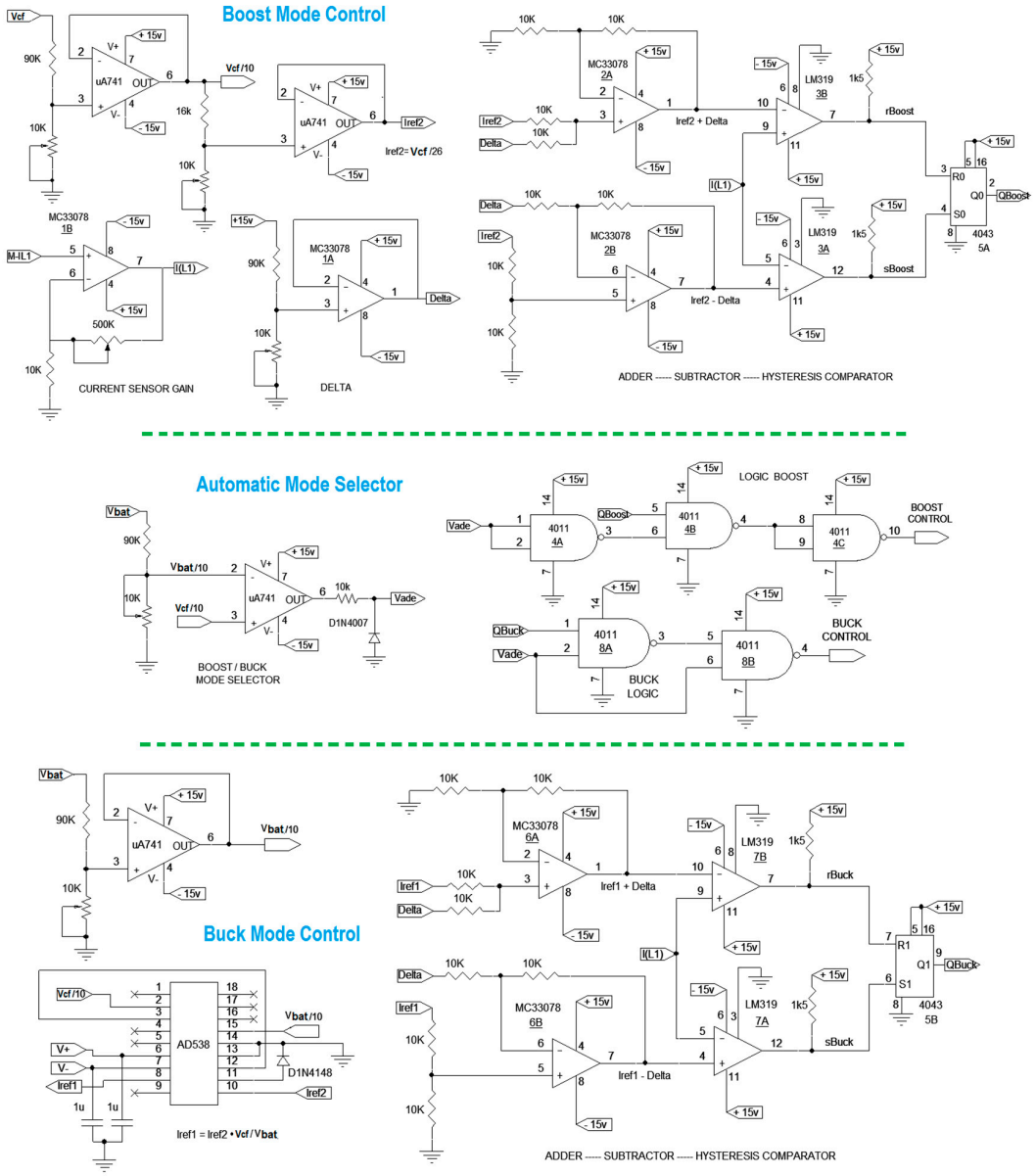

Figure 18. HBB control board.

7. Experimental Verification

The performance of both converters, the hybrid and the Sepic, have been simulated and verified experimentally with two types of input signals. The first signal $v_{\mathrm{p}}(t)$ is the pulse waveform provided by the harvesting device of Figure 8. The simulated results are shown in Figure 19a–f. The second signal $v_{\mathrm{p}}(t)$ is a sinusoidal waveform, and the simulated and experimental results are given in Figure 20a–f. Experimental results with a third pulse waveform are in Figure 21a–d.

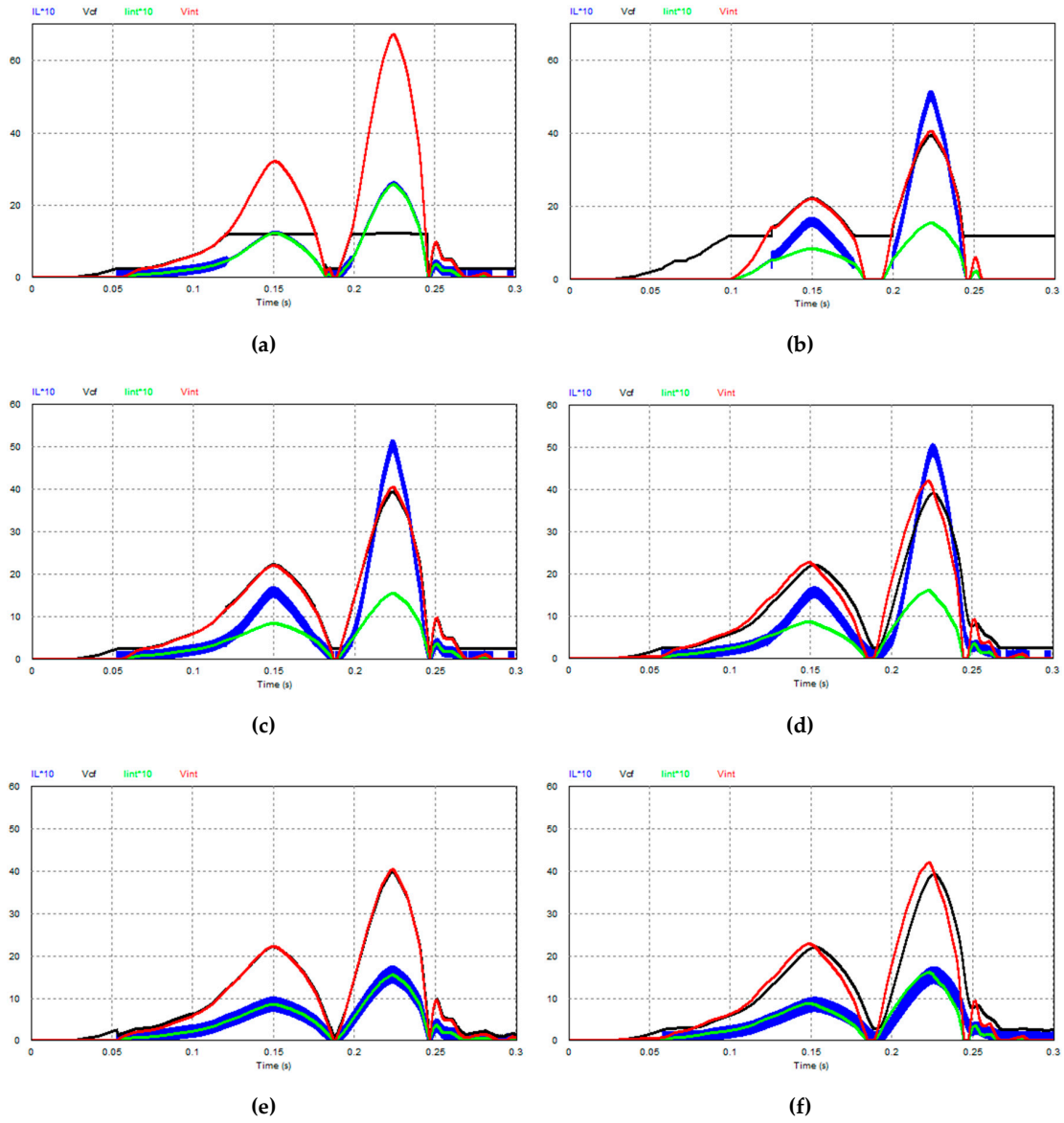

Figure 19. PSIM simulations with a pulse input: (**a**) HBB boost mode C_f = 10 µF, (**b**) HBB buck mode C_f = 10 µF, (**c**) HBB C_f = 10 µF, (**d**) HBB C_f = 200 µF, (**e**) Sepic C_f = 10 µF, (**f**) Sepic C_f = 200 µF.

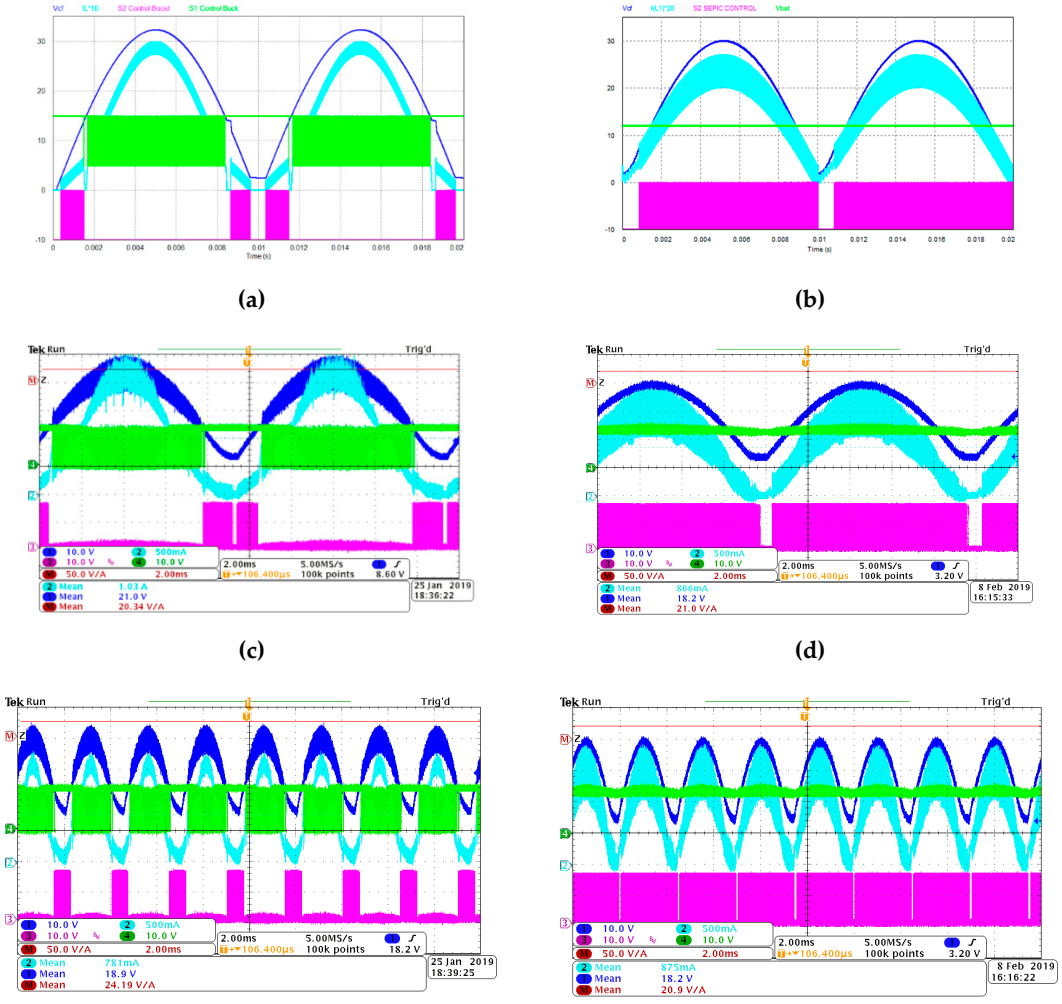

Figure 20. Simulation and experimental tests with C_f = 10 µF, and a sinusoidal input of $v_p(t) = 60{\cdot}sin(2\pi f_o{\cdot}t)$: (**a**) HBB simulation with f_o = 50 Hz, (**b**) Sepic simulation with f_o = 50 Hz, (**c**) HBB prototype with f_o = 50 Hz, (**d**) Sepic prototype with f_o = 50 Hz, (**e**) HBB prototype with f_o = 200 Hz, and (**f**) Sepic prototype with f_o = 200 Hz.

In the simulation captions of Figure 19, the signals shown are: $i_L(t)$ in blue, $v_{cf}(t)$ in black, $i_{int}(t)$ in light green, and finally $v_{int}(t)$ in red. The currents are shown amplified by a factor 10. Current $i_{int}(t)$ is the adaptor input current, this is, the absolute value of the harvesting device current. Signal $v_{int}(t)$ is the absolute value of the harvesting device internal voltage drop, this is $v_{int}(t) = R_{int} \cdot i_{int}(t)$. If impedance matching occurs, then $v_{int}(t)$ must coincide with $v_{cf}(t)$, the adaptor input voltage.

The simulated cases are the following: Figure 19a HBB with only the boost mode enabled; Figure 19b HBB only enabling the buck mode; in cases Figure 19c,d the HBB adaptor can work with both modes, but the capacitor value is C_f = 10 µF in case Figure 19c, and C_f = 200 µF in case Figure 19d; and finally cases Figure 19e,f depict the Sepic converter, using C_f = 10 µF in Figure 19e and with C_f = 200 µF in Figure 19f.

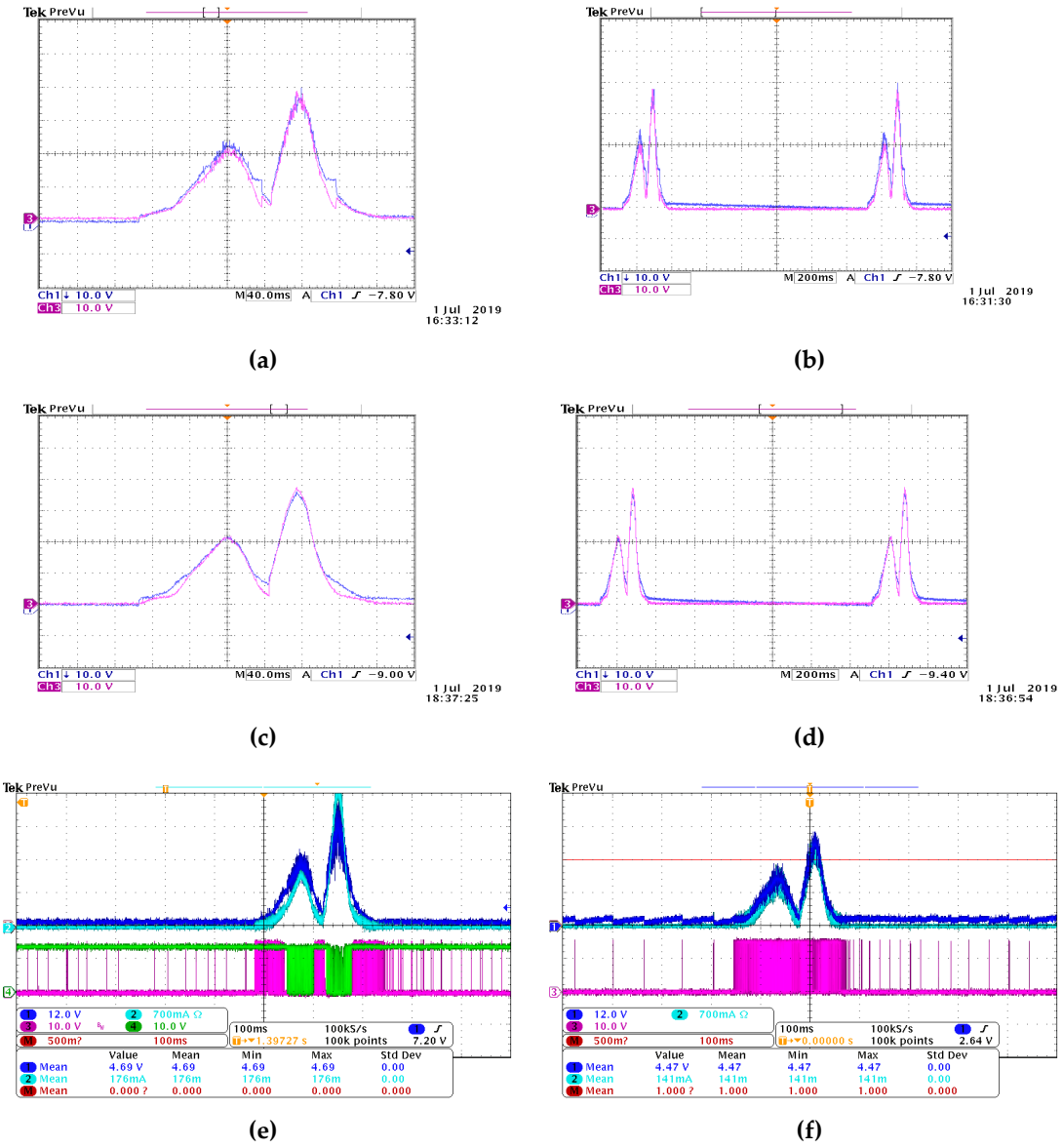

Figure 21. Experimental tests with pulse-train, C_f = 10 µF: (**a**) HBB pulse detail, (**b**) HBB pulse-train, (**c**) Sepic pulse detail, (**d**) Sepic pulse-train, (**e**) HBB with control signals, and (**f**) Sepic with control signals.

As expected, and verified in Figure 19, in the Sepic converter, the adaptor input current $i_{int}(t)$ and the inductor current $i_{L1}(t)$ are equal, but in the HBB converter both currents only coincide in the boost mode, in the buck mode both currents are different. The effect of the C_f filter capacitor can also be observed. When its value is 200 µF, $v_{cf}(t)$ and $v_{int}(t)$ are different. There is a phase shift between them, and therefore the impedance matching is not perfect. Finally, in Figure 19a,b it can be appreciated that impedance matching occurs only when a converter is switching. In the HBB boost mode, the impedance matching only happens when $v_{cf}(t) < Vbat$, see Figure 19a, whereas in the buck mode, impedance matching takes place only when $v_{cf}(t) > Vbat$, as can be seen in Figure 19b.

Figure 20 depicts the simulated and experimental results obtained with a sinusoidal waveform for $v_p(t)$. Both converters have been tested at different frequencies from 50 Hz to 200 Hz. Realize that in a sea wave-train, waves are separated 10–20 seconds, implying a wave-train frequency of 0.05 Hz–0.1 Hz. In this way, a wave pulse can stand for 0.25–2.5 seconds, that corresponds to a range of fundamental frequencies of 0.4 Hz–4 Hz. To assure a good behavior with sea waves, the tests have been made at

unrealistically high frequencies for the harvesting device. If the tests are satisfactory, the $v_{Cf}(t)$ tracking behavior of a real sea-wave pulse voltage $v_p(t)$ will deliver even better results.

The signals shown at Figure 20 are the following: The input adaptor voltage $v_{Cf}(t)$ in shown in dark blue, the inductor current $i_{L1}(t)$ in cyan color, the HBB buck mode switch gate signal $S_{buck}(t)$ is shown light green, and finally the Sepic switch, and the HBB boost mode switch gate signals $S_{sepic}(t)$ and $S_{boost}(t)$ are shown in pink.

The oscilloscope captions at Figure 20c,d corresponding to the real experimental test at 50 Hz show a good agreement with the corresponding simulated results, also at 50 Hz. The experimental results at 200 Hz, show that at his frequency the filtering effect of $C_f = 10$ μF does not allow the adaptor input voltage $v_{Cf}(t)$ to drop at zero volts. Figure 20a shows clearly the dead-zone effect around $V_{bat} = 12$ V, where the HBB operating in boost mode changes to buck operation mode and vice-versa. Comparing the HBB and the Sepic converter experimental results, the adaptor input voltage $v_{Cf}(t)$ exhibit a small ripple in the Sepic case and in the HBB operation mode because the adaptor input current $i_{int}(t)$ is the inductor one $i_{L1}(t)$. Conversely, in the HBB buck mode, the adaptor input current $i_{L1}(t)$ is a pulsating one, and the ripple is higher.

Figure 21 depicts the experimental results using a laboratory programmable power supply that delivers a train of voltage pulses imitating a sea wave-train. Each voltage pulse reproduces the harvesting-device pulse given in Figure 8. This power supply supplies the impedance matching circuit through a series resistor of 26 Ω reproducing the harvesting device output impedance.

The captions in Figure 21a–d show two waveforms. The voltage-drop in the 26 Ω resistance $v_{int}(t)$ is shown in pink color, whereas the impedance matching circuit input voltage $v_{Cf}(t)$ is shown in dark blue color. As can be seen in these figures, there is a good agreement between both curves proving the correct behavior of the impedance matching circuit, for both converters: The HBB and the Sepic converter. The remaining captions, Figure 21e,f, show various signals from the HBB and the Sepic converters, respectively. The signals shown in these captions are: $v_{int}(t)$ in cyan color, $v_{Cf}(t)$ in dark blue, $S_{boost}(t)$ and $S_{sepic}(t)$ in pink color, and finally $S_{buck}(t)$ in light grey.

The input impedance Z_{in}, and the η_M matching efficiency (44) for both converters are depicted in Figure 22a–d. The data shown in these graphs have been obtained along with the sinusoidal experiments of Figure 20. Three different frequencies are used: 50 Hz (red), 100 Hz (blue), and 200 Hz (green). The HBB and the Sepic converter input impedances Z_{in} are plotted, respectively, in Figure 22a,b.

The impedance matching efficiency η_M (44) of both converters is shown Figure 22c,d. That matching efficiency has been defined as the ratio between the power absorbed by the converter, and the power absorbed by the converter in case of an ideal matching, when $Z_{in} = R_{int} = 26$ Ω.

$$\eta_M = \frac{Z_{in} \cdot V_P^2}{(26 + Z_{in})^2} \cdot \frac{(26+26)^2}{26 \cdot V_P^2} = 104 \cdot \frac{Z_{in}}{(26 + Z_{in})^2} \tag{44}$$

This experimental section ends with two photographs given in Figure 23. Thus, Figure 23a shows the experimental workbench testing the HBB converter, whereas Figure 23b show the same environment with the Sepic converter.

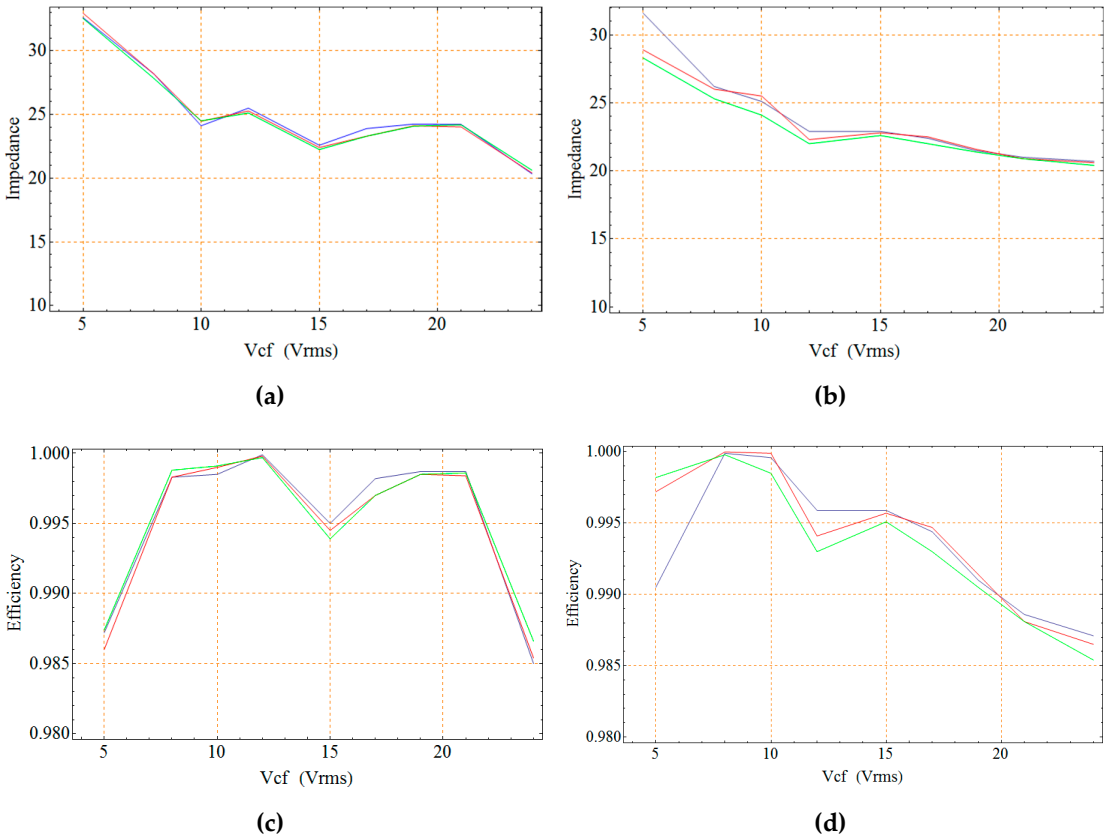

Figure 22. Experimental tests with sinusoidal signals, C_f = 10 µF: (**a**) HBB input impedance, (**b**) Sepic input impedance, (**c**) HBB matching efficiency, and (**d**) Sepic matching efficiency.

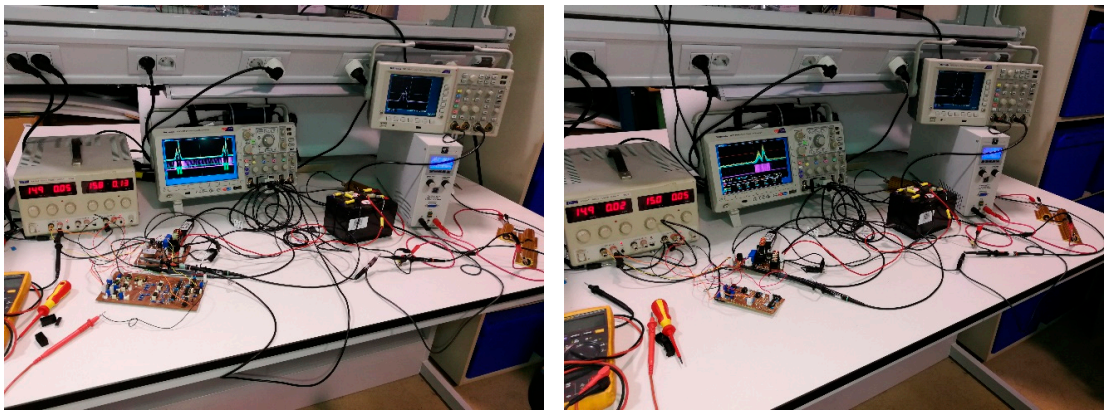

(**a**) (**b**)

Figure 23. Experimental workbench during the test with the eperiment of Figure 22: (**a**) HBB adaptor and (**b**) Sepic adaptor.

8. Conclusions

Although extracting electric power from sea-waves at great scale is worldwide developing, the extraction of small amounts of energy from the waves, conveniently stored in a battery, can be solution to supply small stand-alone equipment, with occasional and short-lived power consumption peaks: Weather stations, telecom relays, and similar equipment.

The design, simulation, realization, and verification of an inductive harvesting generator that profits the differential position of two sea-surface points has been presented. This device supposes a novelty compared to sea-wave energy buoys and harvesting devices based on the vertical oscillation of a single sea point.

The proposed harvesting generator is made with three transducers, that are based on a coil-magnet arrangement, where a permanent magnet moves linearly inside the coil. The generator operation has also been simulated and verified experimentally.

Next, two switching converters, a hybrid buck-boost cell and a Sepic converter have been proposed, analyzed, and verified experimentally as matching circuits to transfer the energy from the harvesting device to the storage 12 V battery. Two different sliding mode control surfaces are required to guarantee the impedance matching using the HBB converter. Thus, during the boost mode the corresponding surface controls the input current, whereas in the buck mode, the surface controls the output current. Conversely, a clear advantage of the Sepic converter is that only a single surface is needed for the same purpose, because in this case the adaptor circuit input current is always the controllable inductor current. Indeed, the Sepic converter control law is the same that has been used for the boost mode operation in the HBB converter.

The main difference between both adaptor circuits is their behavior when the adaptor input voltage $v_{Cf}(t)$ coincides with the battery voltage. While the hybrid converter must change its operation mode, nothing happens with the Sepic converter. In the hybrid converter case, there is an input voltage dead-zone where the converter is not switching. Although the switching losses disappear, as the converter becomes uncontrolled, the impedance matching is lost during those instants.

Both converters behave reasonably well, and show good results matching the generator output impedance and the converter input impedance, as shown in the extensive experimental and simulation results. In both cases, as can be seen in Figure 23a,b there is a slight variation of the adaptor input resistance, due the current sensor lack of linearity working in a wide range of current values, the variable delay caused by the mosfet drivers, and finally the converter efficiency, which is not obviously constant along the input voltage range. Anyway, the matching efficiency is always over 95% whatever be the input voltage, as can be seen in Figure 22c,d.

To reduce the input impedance variation in terms of the input voltage, the hysteresis width used to implement the sliding surfaces by means of hysteretic comparators must be reduced. Nevertheless, although this would increase the tracking precision, leading to a slight increment of the matching efficiency, maybe the switching losses would be greatly increased leading to a global reduction of the energy delivered to the storage battery.

In this paper two switching converters operating as impedance matching circuits have been studied. To achieve this, they must be forced to behave like a loss free resistor, and here sliding mode control is introduced as an easy technique to assure this behavior in a wide range of input and output voltage variations. Buck-boost and similar converters in DCM operation are used in the literature for this proposal, in harvesting applications, but the input voltage variation range is usually small. The solution proposed here allows impedance matching and loss free resistor behavior with harvesting generators with a wide input voltage variation range. The simplicity of the sliding mode control technique, its inherent robustness against parametric variation, and input and output disturbances, are the main advantages of the technique proposed here.

These issues, as other related to a different configuration of the harvesting device coils will be the subject of a future research.

Author Contributions: Conceptualization, J.A.G.-C., and H.V.-B.; methodology, H.V.-B., J.A.G.-C., J.A.B.-R. and À.C.-P.; validation, J.A.G.-C.; formal analysis, H.V.-B. and J.A.G.-C.; investigation, H.V.-B., J.A.G.-C. and J.A.B.-R.; resources, H.V.-B.; writing—original draft preparation, J.A.G.-C., and H.V.-B.; writing—review and editing, H.V.-B., J.A.G.-C., J.A.B.-R, and À.C.-P.; visualization, J.A.G.-C. and À.C.-P.; supervision, H.V.-B.; project administration, H.V.-B.; funding acquisition, H.V.-B.

Funding: This research was funded by the Spanish Agencia Estatal de Investigación (AEI) and the Fondo Europeo de Desarrollo Regional (FEDER) under research projects DPI2015-67292-R (AEI/FEDER, UE).

Conflicts of Interest: The authors declare no conflict of interest.

References

1. Falcao, A.F. Wave energy utilization: A review of the technologies. *Renew. Sustain. Energy Rev.* **2010**, *14*, 900–915. [CrossRef]
2. Faiz, J.; Nematsaberi, A. Linear electrical generator topologies for direct-drive marine wave energy conversion—An overview. *IET Renew. Power Gener.* **2017**, *11*, 1163–1176. [CrossRef]
3. Phillips, O.M. *The Dynamics of the Upper Ocean*; Cambridge University Press: Cambridge, UK, 1977; ISBN 0-521-29801-6.
4. Herbich, J.B. *Handbook of Coastal Engineering*; McGraw-Hill: New York, NY, USA, 2000; ISBN 978-0-07-134402-9.
5. Bou-Mosleh, C.; Rahme, P.; Beaino, P.; Mattar, R.; Nassif, E.A. Contribution to Clean Energy Production using a Novel Wave Energy Converter. In Proceedings of the 2nd Renewable Energy for Developing Countries—REDEC 2014, Beirut, Lebanon, 26–27 November 2014; pp. 108–111.
6. Karayaka, H.; Mahlke, H.; Bogucki, D.; Mehrubeoglu, M. A Rotational Wave Energy Conversion System Development and Validation with Real Ocean Wave Data. In Proceedings of the 2011 IEEE Power and Energy Society General Meeting, Detroit, MI, USA, 24–28 July 2011.
7. Liang, H.; Zhang, D.; Yang, J.; Tan, M.; Huang, C.; Wang, J.; Chen, Y.; Xu, C.; Sun, K. Hydrodynamic research of a novel floating type pendulum wave energy converter based on simulations and experiments. In Proceedings of the OCEANS 2016, Shanghai, China, 10–13 April 2016.
8. Tasneem, N.; Suri, S.; Mahbub, I. A low-power CMOS voltage boosting rectifier for wireless power transfer applications. In Proceedings of the 2018 Texas Symposium on Wireless and Microwave Circuits and Systems (WMCS), Waco, TX, USA, 5–6 April 2018.
9. Belal, E.; Mostafa, H.; Ismail, Y.; Said, M. A Voltage Multiplying AC/DC Converter for Energy Harvesting Applications. In Proceedings of the 2016 28th International Conference on Microelectronics (ICM), Giza, Egypt, 17–20 December 2016; pp. 229–232.
10. Cheng, S.; Jin, Y.; Rao, Y.; Arnold, D. An Active Voltage Doubling AC/DC Converter for Low-Voltage Energy Harvesting Applications. *IEEE Trans. Power Electron.* **2011**, *26*, 2258–2265. [CrossRef]
11. Haoyu, W.; Yichao, T.; Khaligh, A. A Bridgeless Boost Rectifier for Low-Voltage Energy Harvesting Applications. *IEEE Trans. Power Electron.* **2013**, *28*, 5206–5214.
12. Sun, Q.; Patil, S.; Stoute, S.; Sun, N.; Lehman, B. Optimum design of magnetic inductive energy harvester and its AC-DC converter. In Proceedings of the 2012 IEEE Energy Conversion Congress and Exposition (ECCE), Raleigh, NC, USA, 15–20 September 2012; pp. 394–400.
13. Lefeuvre, E.; Audigier, D.; Richard, C.; Guyomar, D. Buck-Boost Converter for Sensorless Power Optimization of Piezoelectric Energy Harvester. *IEEE Trans. Power Electron.* **2007**, *22*, 2018–2025. [CrossRef]
14. Guo, T.; Lerley, R.; Ha, D.S. Development of a power conditioning circuit for railcar energy harvesting. In Proceedings of the MWSCAS—The 56th international Midwest Symposium on Circuits and Systems, Columbus, OH, USA, 4–7 August 2013; pp. 513–516.
15. Chen, N.; Wei, T.; Dong, H.; Jung, H.J.; Lee, S. Alternating Resistive Impedance Matching for an Impact-Type Micro-Wind Piezoelectric Energy Harvester. *IEEE Trans. Ind. Electron.* **2018**, *65*, 7374–7382. [CrossRef]
16. Sun, Q.; Patil, S.; Sun, N.; Lehman, B. Phase/RMS Maximum Power Point Tracking for Inductive Energy Harvesting System. In Proceedings of the 2015 IEEE Energy Conversion Congress and Exposition (ECCE), Montreal, QC, Canada, 20–24 September 2015; pp. 408–413.
17. Heo, S.; Yang, Y.; Lee, J.; Lee, S.; Kim, J. Micro Energy Management for Energy Harvesting at Maximum Power Point. In Proceedings of the 2011 International Symposium on Integrated Circuits, Singapore, 12–14 December 2011; pp. 136–139.
18. Shousha, M.; Dinulovic, D.; Haug, M. A universal topology based on buck-boost converter with optimal resistive impedance tracking for energy harvesters in battery powered applications. In Proceedings of the 2017 IEEE Applied Power Electronics Conference and Exposition (APEC), Tampa, FL, USA, 26–30 March 2017; p. 2111.

19. Cid-Pastor, A.; Martínez-Salamero, L.; el Aroudi, A.; Giral, R.; Calvente, L.; Leyva, R. Synthesis of Loss-Free Resistors based on sliding-mode control and its applications in power processing. *Control Eng. Pract.* **2013**, *21*, 689–699. [CrossRef]
20. Griffith, D. *Introduction to Electrodynamics*, 3rd ed.; Pearson: London, UK, 2013; ISBN 978-0-321-85656-2.
21. Singer, S.; Ozeri, S.; Shmilovitz, D. A Pure Realization of Loss-Free Resistor. *IEEE Trans. Circuits Syst. I Regul. Pap.* **2004**, *51*, 1639–1647. [CrossRef]